PCCP

PAPER

View Article Online
View Journal | View Issue

Cite this: *Phys. Chem. Chem. Phys.*, 2024, **26**, 28495

Insight into physico-chemical properties of oxalatoborate-based ionic liquids through combined experimental-theoretical characterization†

Matteo Palluzzi, [a] Giorgia Mannucci, [a] Akiko Tsurumaki,[ab] Matteo Busato, [a] Maria Assunta Navarra *[ab] and Paola D'Angelo *[a]

Received 5th June 2024,
Accepted 31st October 2024

DOI: 10.1039/d4cp02296c

rsc.li/pccp

Ionic liquids (ILs) including oxalatoborate anions, like bis(oxalato)borate (BOB) and difluoro(oxalato)borate (DFOB) are extensively used in the battery sector as additives to promote the formation of protective layers on the surface of high-voltage cathode materials. In this work four ILs have been synthesized: *N*-ethoxyethyl-*N*-methyl piperidinium bis(oxalato)borate ($PIP_{1,2O2}BOB$), *N*-ethoxyethyl-*N*-methylpiperidinium difluoro(oxalato)borate ($PIP_{1,2O2}$ DFOB), *N*-propyl-*N*-methylpiperidinium bis(oxalato)borate ($PIP_{1,3}BOB$) and *N*-propyl-*N*-methylpiperidinium difluo ro(oxalato)borate ($PIP_{1,3}DFOB$) and their thermal properties have been linked to their structure. The presence of an oxygen atom in the $PIP_{1,2O2}$ lateral chain suppresses crystallization of the ILs. Furthermore, $PIP_{1,2O2}DFOB$ shows a lower glass transition temperature than $PIP_{1,2O2}BOB$. These observations have been explained using a combined molecular dynamics and density functional theory approach and an increase in the degree of freedom of the lateral chain of the cation due to the ether oxygen has been found. Comparing $PIP_{1,2O2}DFOB$ and $PIP_{1,2O2}BOB$, a notable interaction between different domains of the anions is observed and is stronger in the DFOB case due to the charge-delocalization induced by the fluorine atoms, which generates a relatively positive charge on the boron atom. This is correlated to the weaker cation–anion attraction which hinders the glass transition of $PIP_{1,2O2}DFOB$.

1 Introduction

Ionic liquids (ILs) are a class of materials defined as salts with a melting point below 100 °C.[1–3] They are usually composed of a bulky organic cation (such as ammonium, imidazolium, pyrrolidinium, or piperidinium) and an anion having a strong delocalized charge and/or structural flexibility,[3] hindering the crystallization and lowering the melting point (T_m). In recent years ILs have received increasing attention in many different research fields such as organic/inorganic synthesis,[4,5] biomass treatment,[6] metallurgy processes,[7] gas absorption,[8] and energy storage technologies.[3] Behind this interest are the series of beneficial properties of ILs: low flammability, low vapor pressure, notable thermal and electrochemical stability, and good ionic conductivity.[3] Due to the strong relationship between the physicochemical properties and the structure of ILs, it is possible to design an enormous number of ILs for specific tasks by finely tuning the structure of the cations and anions.

In the field of energy storage, particularly in the battery sector, a significant amount of research is dedicated to the development of new materials. The goal is to create batteries that can meet modern societal demands, especially for use in electric and hybrid vehicles (E/HV) and for storing energy produced by renewable sources. The next generation of batteries should offer increased energy density, a long calendar life (both crucial for large-scale energy storage), and fast-charging capabilities (important for E/HV applications). Additionally, these batteries must meet strict requirements for safety, environmental compatibility, and low cost. Due to their intrinsic properties, ILs are considered a promising class of materials to help achieve these goals.

Currently, ILs are mainly used in batteries as substitutes or additives for the carbonate-based solvents found in electrolytes.[9–13] The ILs used as replacement, *i.e.*, the main solvent, commonly employ bis(trifluoromethanesulfonyl)imide (TFSI) or bis(fluorosulfonyl)imide (FSI) (Fig. S1a and b, ESI†) as the anion because they provide low viscosity and good ionic conductivity, which are the most important features for the electrolyte. Additionally, a widely employed strategy for electrochemical application is the introduction of an ether group in the lateral chain of the IL cation. The presence of the ether oxygen

[a] *Department of Chemistry, Sapienza University of Rome, P.le A. Moro 5, 00185, Rome, Italy. E-mail: p.dangelo@uniroma1.it, mariassunta.navarra@uniroma1.it*
[b] *Hydro-Eco Research Center, Sapienza University of Rome, Via A. Scarpa 16, 00161 Rome, Italy*

† Electronic supplementary information (ESI) available: ATR-FTIR spectra, additional DSC curves, dihedral angle distribution functions, radial distribution functions, and additional computational details. See DOI: https://doi.org/10.1039/d4cp02296c

increases the cation degrees of freedom leading to a hindered or totally suppressed crystallization of the ILs,[14–19] that is advantageous for the battery usage at low temperatures. In contrast, when ILs are used as the additives, their viscosity and T_m are not of primary importance, and alternatively their main role becomes providing new functions to the system. First, the addition of ILs can improve the thermal and electrochemical stability of the electrolyte.[20,21] Second, ILs can participate in the formation of protective electrode/electrolyte interphases (EEIs) through their decomposition, reducing side effects that could lead to the failure of the battery.[16,22–24] Following this path, in recent years, new anions have been employed to obtain ILs able to form protective cathode solid electrolyte interphases (CEI). Bis(oxalato)borate (BOB) and difluoro(oxalato)borate (DFOB) (Fig. S1c and d, ESI†) are two promising anions due to their ability to efficiently form a CEI on the surface of high-voltage cathode materials, such as the $LiNi_{0.5}Mn_{1.5}O_4$ (LNMO) spinel, improving their capacity retention upon cycling.[16,22] Consequently, it is foreseeable that ILs based on these peculiar anions will have an important role in the future, since the use of high-voltage cathode materials is the key for the development of batteries with higher energy density.

However, the number of structural studies on oxalatoborate-based ILs available in literature is limited,[22,25–27] despite their importance to get insight into their intrinsic properties. In the present study we have carried out a combined experimental and computational investigation on the effect of the insertion of an ether oxygen in the lateral chain of the cation of the IL formed with the BOB and DFOB anions. In particular, four ILs have been synthesized and characterized experimentally by infrared spectroscopy and differential scanning calorimetry (DSC). At the same time, a computational study, involving both classical molecular dynamics (MD) simulations and density functional theory (DFT) calculations, has been carried out to profoundly comprehend the experimental results and to provide an explanation on the relationship between the observed thermal behavior of the ILs and the interactions between the component ions.

2 Experimental and theoretical methods

2.1 Synthesis of the ILs

N-Methylpiperidine, 2-bromoethyl ethyl ether, 1-bromopropane, lithium bis(oxalato)borate (LiBOB), and lithium difluoro(oxalato) borate (LiDFOB) were all purchased from Merck KGaA (Darmstadt, Germany) and used as received. Two bromide salts, namely *N*-ethoxyethyl-*N*-methylpiperidinium bromide ($P_{1,2O2}Br$) [^{1}H-NMR (300 MHz, DMSO-d_6, δ/ppm relative to Me_4Si): 1.12 (3H, t, J = 6.9, OCH_2CH_3), 1.54 (2H, m, $N(CH_2)_2(CH_2)_2CH_2$), 1.79 (4H, m, $N(CH_2)_2(CH_2)_2$), 3.09 (3H, s, NCH_3), 3.39 (4H, m, $N(CH_2)_2(CH_2)_2$), 3.49 (2H, q, J = 6.9, OCH_2CH_3), 3.60 (2H, t, J = 4.9, NCH_2CH_2), 3.80 (2H, t, J = 4.5, NCH_2CH_2)] and *N*-propyl-*N*-methylpiperidinium bromide ($PIP_{1,3}Br$), were synthesized through a quaternization reaction as reported in a previous paper.[22] Once purified through recrystallization, a metathesis reaction has been performed to replace the bromide anion with BOB or DFOB anion. The bromide salts were mixed with LiBOB or LiDFOB (using a molar ratio of Br : Li = 1.1 : 1.0) in Milli-Q water and the resulting ILs were extracted using dichloromethane. The extraction procedure was repeated three times and the three collected organic phases were put all together. To purify the ILs, the organic phase was rinsed with Milli-Q water three times and then passed in a column filled with aluminum oxide (activated, neutral, Brockmann I). The absence of bromide anion impurities was confirmed by checking the absence of silver halide precipitate when the ILs were mixed with $AgNO_3/HNO_3$. A schematic representation of the IL synthesis is reported in Fig. S2 (ESI†). Samples were dried by a rotary evaporator, vacuum dried at 60 °C overnight and finally stored in an Ar-filled glovebox with a content of water below 10 ppm. Using the same procedure four pure ILs (reported in Fig. 1) were prepared: *N*-propyl-*N*-methylpiperidinium bis(oxalato)borate ($PIP_{1,3}BOB$) [IR: 706, 758, 880, 940, 981, 1000, 1074, 1091, 1132, 1212, 1286, 1308, 1774, 1798 cm^{-1}], *N*-propyl-*N*-methylpiperidinium difluoro(oxalato)borate ($PIP_{1,3}DFOB$) [IR: 517, 568, 684, 711, 758, 826, 877, 934, 1076, 1121, 1148, 1226, 1343, 1480, 1760, 1793, 1830 cm^{-1}], *N*-ethoxyethyl-*N*-methylpiperidinium bis(oxalato)borate ($PIP_{1,2O2}BOB$) [IR: 704, 874, 942, 986, 1088, 1130, 1202, 1275, 1301, 1470, 1778, 1801 cm^{-1}], *N*-ethoxyethyl-*N*-methylpiperidinium difluoro(oxalato)borate ($PIP_{1,2O2}DFOB$) [IR: 519, 573, 685, 710, 828, 876, 938, 989, 1077, 1124, 1148, 1180, 1227, 1345, 1472, 1760, 1793, 1828 cm^{-1}].

2.2 Physico-chemical characterization

Attenuated total reflectance Fourier transform infrared (ATR-FTIR) spectra of the ILs was recorded using a Bruker Alpha spectrometer equipped with a germanium crystal and reported in Fig. S3 (ESI†). The investigated range was 500–2000 cm^{-1} with a resolution of 4 cm^{-1}. All the procedures were carried out in the Ar-filled glovebox. Differential scanning calorimetry (DSC) using a Mettler-Toledo DSC 821 was performed in an 80 mL min^{-1} nitrogen flux. The samples were cooled from room temperature to −120 °C with a rate of −5 °C min^{-1} and kept at −120 °C for 5 min to equilibrate the temperature. The heating scan was then recorded from −120 to 120 °C with a rate of 5 °C min^{-1}.

The experimental density of the $PIP_{1,2O2}BOB$, $PIP_{1,2O2}DFOB$ and $PIP_{1,3}DFOB$ was evaluated by filling a 1 mL flask and weighing it.

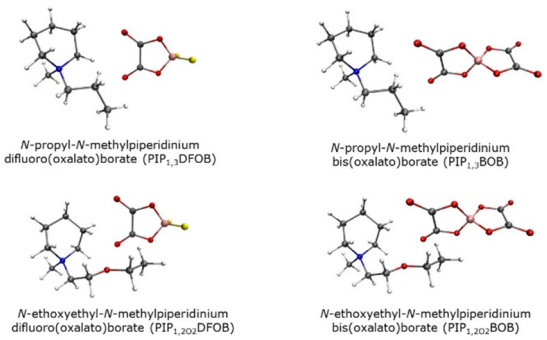

Fig. 1 Cation and anion structures of the four synthesized ILs.

2.3 Computational details

Classical MD simulations were carried out on the $PIP_{1,2O2}BOB$, $PIP_{1,2O2}DFOB$, and $PIP_{1,3}DFOB$ systems. The PACKMOL package was used to build cubic boxes with ~50 Å side length and a number of species chosen in order to reproduce the experimental density.[28] Details about the studied systems are reported in Table S1 (ESI†). The particle mesh Ewald method was used to calculate the long-range electrostatic forces and a cutoff radius of 12 Å was chosen for all the non-bonded interactions.[29,30] Structures and interactions of the $PIP_{1,3}$, $PIP_{1,2O2}$, DFOB, and BOB ions were represented by the all-atom optimized potentials for liquid simulations (OPLS-AA) force field and by the OPLS-compatible parameters developed by Canongia Lopes and Padua.[31,32] New partial charges were parametrized using the CHELPG scheme from DFT optimizations of the isolated ions at the B3LYP/def2TZVP level of theory.[33,34] Each system was first equilibrated in the NVT ensemble for 10 ns following a heating ramp from 300 K to 500 K, and gradually cooling down to 300 K. The data analysis was carried out on a production run of 50 ns in NVT conditions at 300 K. This simulation protocol was previously shown to be appropriate for systems with slow dynamics like ILs and deep eutectic solvents.[35–40] Cross-terms for the Lennard-Jones interaction were constructed with the Lorentz–Berthelot combining rules and the Nosè–Hoover thermostat, with a relaxation constant of 0.5 ps, was employed to control the temperature. Moreover, the leap-frog algorithm with a time step of 1 fs was used to integrate the equation of motion and the LINCS algorithm was employed to constrain all the stretching vibrations involving hydrogen atoms.[41] All the simulations were performed with the Gromacs 2020.6 program.[42] The obtained trajectories were analyzed with the TRAVIS package,[43] while the VMD 1.9.3 software was used for visualization.[44]

To identify and quantify the noncovalent interactions among the components, geometry optimizations were also carried out on $PIP_{1,2O2}DFOB$ and $PIP_{1,2O2}BOB$ clusters composed by two cations and two anions at the B3LYP/6-31+G(d) level of theory. This functional and basis set combination was previously found to offer a good balance between computational cost and accuracy for ILs modeling.[45–47] Frequency calculations were performed for the located stationary points to confirm their nature of true minima. For each cluster, the cation–anion and anion–anion interactions were analyzed with the recently developed independent gradient model (IGM) method.[48–50] IGM takes advantage of a new δg descriptor, which computes the difference between a non-interacting model (the IGM) represented by a virtual upper limit of the electron density gradient $|\nabla\rho^{IGM}|$, and the true electron density gradient $|\nabla\rho|$ representing the real system. The sign of the second eigenvalue of the electron density Hessian matrix $(\mathrm{sign}(\lambda_2)\rho)$ is used to distinguish between non-bonding interactions ($\lambda_2 > 0$) and attractive interactions ($\lambda_2 < 0$). The type of interaction is represented with color coding: blue indicates attractive interactions, green signifies weakly non-bonding or attractive interactions, and red denotes non-bonding situations. The GAUSSIAN 16 package[33] was employed for all DFT simulations.

3 Results and discussion

3.1 Physico-chemical characterization of ILs

The thermal behavior of the four ILs was investigated by DSC measurements (Fig. 2). In the case of $PIP_{1,3}BOB$, which is solid at room temperature, a second-round scan was performed. In the first scan, the T_m was measured at 76.0 °C, while in the second scan (Fig. S4, ESI†) only a glass-transition (T_g) was observed at −26.8 °C. This behavior is due to supercooling, a quite common phenomenon in ILs.[16,51,52] $PIP_{1,3}DFOB$ showed instead both T_g and T_m in the first scan, the former at −69.3 °C and the latter at 14.2 °C. In addition, between T_g and T_m, an endothermic peak was observed, which relates to solid–solid transition, *i.e.*, the transformation of solid state to a *meta* stable phase before its melting. As far as the ILs with an ether group in the lateral chain is concerned, both show only a glass-transition at −32.6 °C and −69.9 °C for $PIP_{1,2O2}BOB$ and $PIP_{1,2O2}DFOB$, respectively. The absence of crystallization even at sub-zero temperatures in the ether-functionalized ILs is explainable by considering the higher number of degrees of freedom of the lateral chain, which hinders and makes impossible an efficient packaging of the ions in the time range of the experiment.

Comparison between BOB- and DFOB-based ILs highlights the lowered T_m and T_g in the DFOB-based ILs as compared to the equivalent BOB-based ones. A similar behaviour has been already observed in the literature in the case of

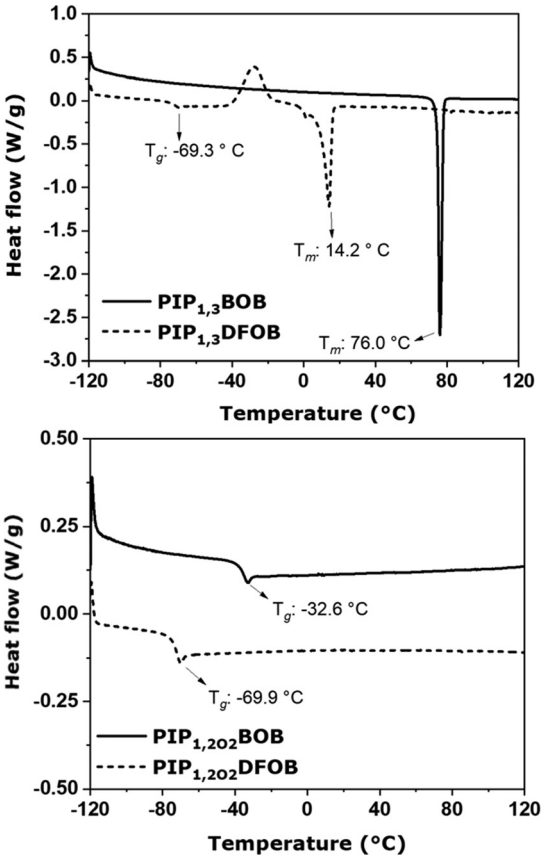

Fig. 2 DSC curves of the four ILs. Only the first scan is reported.

bis(trifluoromethansulfonyl)imide (TFSI) and bis(fluorosulfonyl) imide (FSI) -based ILs, as compared to bis(methanesulfonyl)imide, and explained considering the negative charge delocalization caused by the anion flourination.[53]

The charge delocalization present in the fluorinated compounds causes a weaker anion–cation interaction, which in turn leads to lower T_m and T_g values. On the other hand, when PIP_{13}- and $PIP_{1,2O2}$-based ILs are compared, it can be noticed that the T_g value changes when the cations are combined with BOB, while it remains constant when they are combined with DFOB (−69.3 °C and −69.9 °C, for PIP_{13} and $PIP_{1,2O2}$, respectively).

This trend has been found in previous studies where different BOB/DFOB-based ILs with a pyrrolidinium or piperidinium cation were compared.[16,22,54–56] This suggests that glass transition of BOB-based ILs is heavily influenced by cation while that of DFOB-based ILs strongly depends on the anion due to its strong charge delocalization. This makes the T_g DFOB-based ILs almost unrelated to the functionalization of the side-chain of the cation.

3.2 MD simulations and DFT calculations

While the above considerations regarding the thermal behavior of the ILs are widely supported by structural studies for TFSI and FSI anions, to the best of our knowledge this is not the case for BOB and DFOB anions. Consequently, to investigate the relationship between their physico-chemical properties and structure, MD simulations were performed on the $PIP_{1,2O2}$BOB, $PIP_{1,2O2}$DFOB, and $PIP_{1,3}$DFOB systems. To have accurate information about the tridimensional arrangement of the IL components, spatial distribution functions (SDFs) for the single constituents were calculated from the MD trajectories. Note that, to carry out a quantitative comparison among the isosurfaces of the different ILs, the SDFs are shown with the same density/maximum ratio. The employed isovalues are reported in Table S3 (ESI†). The SDFs computed around the cations for the $PIP_{1,3}$DFOB and $PIP_{1,2O2}$DFOB systems are reported in Fig. 3. They encompass both the center of mass (C.O.M.) of the cation and of the anion as observed centers, plus the oxygen and fluorine atoms of the DFOB and BOB anions, which can give insights on more specific interactions. As it can be observed, the distribution of the quoted species shows a higher number of high probability spots around the cation in the $PIP_{1,2O2}$DFOB case (Fig. 3b). This suggests a greater amount of possible configurations compared to the $PIP_{1,3}$DFOB IL, where the SDFs around the cation show a more ordered distribution of alternated cation–anion–cation shells (Fig. 3a). The more irregular distribution evidenced by $PIP_{1,2O2}$DFOB could arise from the conformational flexibility induced by the oxygen atom in the side chain of the cation. To confirm this hypothesis, we calculated the distribution functions reported in Fig. S5 (ESI†), which are referred to the N–C_1–C_2–C_3 dihedral angle for the $PIP_{1,3}$ cation and the N–C_1–C_2–O dihedral angle for the $PIP_{1,2O2}$ one (Fig. S6, ESI†). For $PIP_{1,2O2}$BOB and $PIP_{1,2O2}$DFOB two peaks are present, which are related to two different configurations of the side chain, while in the case of $PIP_{1,3}$DFOB only one

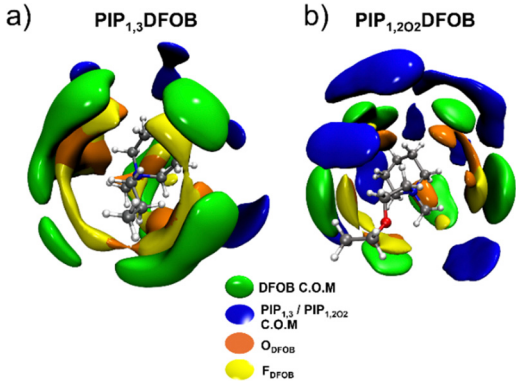

Fig. 3 SDFs around the cations and employed color code for the observed species calculated from the MD simulations of (a) $PIP_{1,3}$DFOB and (b) $PIP_{1,2O2}$DFOB. Isosurfaces have been drawn with the same density/maximum ratio according to the isovalues listed in Table S3 (ESI†). C.O.M is the center of mass of the referred cation/anion.

configuration is found. The increased structural disorder due to multiple possible conformations of the side-chain in $PIP_{1,2O2}$DFOB can well-explain the absence of an observable crystallization behavior in the ether-functionalized ILs, due to the increased difficulty in realizing an efficient packaging of the ions. This makes the use of these ILs extremely appealing for the application in batteries even at low temperatures, similarly to other IL-based electrolytes.[57]

Fig. 4 shows a comparison of the SDFs calculated for the $PIP_{1,2O2}$DFOB and $PIP_{1,2O2}$BOB systems employing the anion as reference. It is noteworthy that for $PIP_{1,2O2}$DFOB (Fig. 4a), besides the probability spots relative to the cation C.O.M. that stem from the traditional cation–anion–cation distribution of ILs bulk, isosurfaces relative to the observed DFOB anions are also found very close to the reference. In particular, those corresponding to the observed carbonyl oxygen (O) and F atoms of the DFOB anion are highly localized. Note that, when speaking about ILs, the constituents can be better described as molecular ions with a highly delocalized charge, thus being constituted by partially positive and negative domains, rather than by point-like charges. To better visualize this, the electrostatic potential maps of the single ions were calculated from DFT calculations and are reported in Fig. S7 (ESI†). The strong charge delocalization effect of the fluorine atoms can induce the formation of a recognizable positive charge on the boron center of DFOB (see the calculated partial charges in Table S2, ESI†). An attractive interaction among different regions of the anions could therefore explain the evidence obtained by the SDFs in Fig. 4a. These interactions likely take part in the overall structural arrangement of the IL bulk, alongside and in competition with the canonical cation–anion attraction. Considering instead $PIP_{1,2O2}$BOB, the SDFs computed around the anion show less localized spots relative to the observed BOB anions (Fig. 4b). This is likely due to the different structure of this anion, which, contrarily to the DFOB one, carries no fluorine atoms and therefore shows less presence of partially positive and negative domains in its molecular structure. The whole

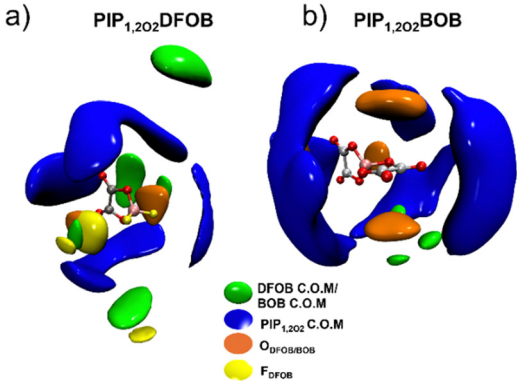

Fig. 4 SDFs around the anion and employed color code for the observed species calculated from the MD simulations of (a) $PIP_{1,2O2}DFOB$ and (b) $PIP_{1,2O2}BOB$. Isosurfaces have been drawn with the same density/maximum ratio according to the isovalues listed in Table S3 (ESI†). C.O.M is the center of mass of the referred cation/anion.

result is a weaker cation–anion attraction in the $PIP_{1,2O2}DFOB$ IL compared to the $PIP_{1,2O2}BOB$ one, because of a higher competitive anion–anion interaction. This can be well correlated with the reduced T_m and T_g values of the DFOB-based ILs as compared to their BOB-based equivalents.

To get further insights into the different degree of structural disorder, pair radial distribution functions ($g(r)$'s) have been calculated from the MD simulations for the $PIP_{1,2O2}DFOB$ and $PIP_{1,2O2}BOB$ systems and are reported in Fig. S8 (ESI†). Note that the $g(r)$'s have been multiplied by the numerical density of the observed species (ρ) since the mere $g(r)$'s can be misleading when comparing systems with different composition. The $g(r)$ related to the cation–anion distribution (Fig. S8a, ESI†) shows the presence of a broad first peak centered at ~5.8 Å for $PIP_{1,2O2}DFOB$, while for $PIP_{1,2O2}BOB$ a myriad of more defined peaks is observed between 4.0 and 9.0 Å. The same is true for the cation–cation distribution in Fig. S8b (ESI†). The presence of defined multiple peaks in a $g(r)$ can arise from multiple configurations and is a sign of a noticeable structural order, akin to crystals, and provides evidence for an increase in the ordering of cations and anions in BOB-based ILs. Differently, the convolution into a smaller number of broad peaks is peculiar of disordered liquid systems.[35,38] In general, in an IL, an efficient packing of the ionic system is obtained when strong coulombic interactions are present, giving rise to a high degree of structural order. Therefore, the obtained results suggest that the reduced cation–anion interaction in DFOB-based ILs increases their structural disorder, making more difficult their crystallization and glass-transition.

To definitely prove this hypothesis about the stronger anion–anion interplay in the DFOB-based ILs, which causes weaker cation–anion interactions, we performed the IGM analysis on the $PIP_{1,2O2}DFOB$ and $PIP_{1,2O2}BOB$ clusters each composed by two cations and two anions, optimized at DFT level. Note that at least two ionic couples were included to take into account the many-body effects provided by the cation. Differently, the repulsive forces between two gas-phase anions would be too strong to study an eventual anion–anion interaction. The results are reported in Fig. 5 for the anion–anion interactions and in Fig. 6 for the cation–anion one. In Fig. 5a and c we report the isosurfaces representing the IGM descriptor for noncovalent intermolecular interactions (δg^{inter}) obtained for the DFOB–DFOB and BOB–BOB anions, respectively. The obtained surfaces show that there are attractive noncovalent interactions between the anions in both ILs. These interactions are more favorable in $PIP_{1,2O2}DFOB$ than in $PIP_{1,2O2}BOB$, as evidenced by the presence of a localized blue spot in the green isosurface that is due to the existence of a stronger interaction in that region of space (see the color-code reported in Fig. 5). The equivalent analysis is shown in the plots of Fig. 5b and d for $PIP_{1,2O2}DFOB$ and $PIP_{1,2O2}BOB$, respectively. Here, negative values in the abscissa indicate an attractive interaction, while positive values are connected with the repulsive part of the δg^{inter} descriptor. Two sharp spikes, one at negative and one at positive values, are present for both the DFOB–DFOB and BOB–BOB systems. However, the spike connected with the attractive interaction shows a higher intensity than that connected with the repulsive interaction in both cases. The whole result strongly suggests that a favorable interaction is possible among different domains of the anions in both the $PIP_{1,2O2}DFOB$ and $PIP_{1,2O2}BOB$ ILs, irrespectively of their overall negative charge. In addition, the peak referred to the repulsive part is less intense in the DFOB–DFOB case with respect to the BOB–BOB one, while those relative to the attractive region have similar intensities. As the difference between the intensity of the repulsive and attractive part is related to the strength of the interaction,[41,42,47] this result confirms the stronger attraction among the anions in the DFOB-based IL.

Fig. 6 exhibits the IGM analysis performed for the cation–anion interaction in the $PIP_{1,2O2}DFOB$ and $PIP_{1,2O2}BOB$ ILs, respectively. As expected, in both cases the interactions have a markedly attractive nature, as the color-spot connected with the non-covalent interactions are quite spread (Fig. 6a and b). In Fig. 6c we report the overlapping plots for the attractive

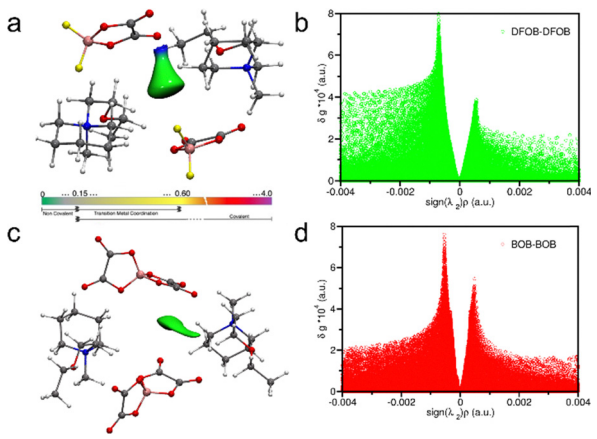

Fig. 5 Minimum energy structures with color-filled δg_{inter} surfaces according to the reported color-code and corresponding δg_{inter} plot referred to the anion–anion interactions for the $PIP_{1,2O2}DFOB$ ((a) and (b)) and $PIP_{1,2O2}BOB$ ((c) and (d)) clusters.

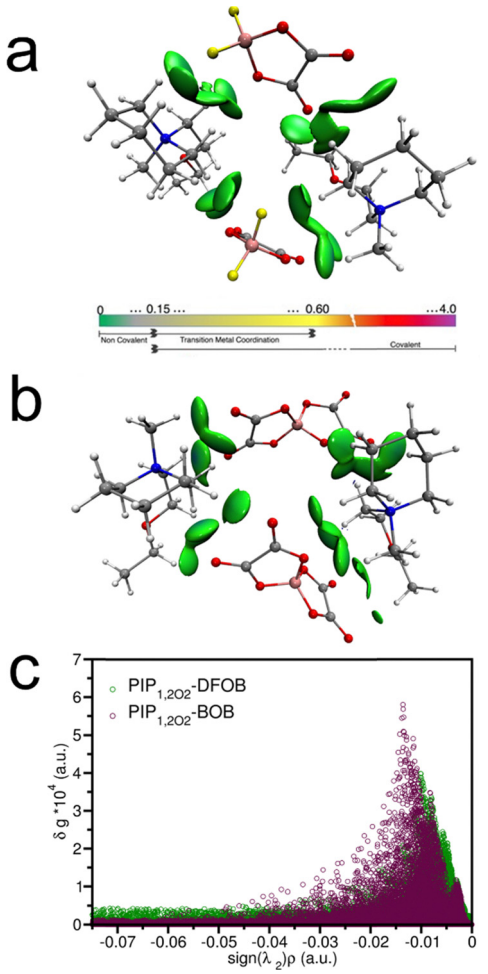

Fig. 6 Minimum energy structures with color-filled δg_{inter} surfaces according to the reported color-code for the (a) $PIP_{1,2O2}$DFOB and (b) $PIP_{1,2O2}$BOB clusters and (c) corresponding attractive part of the δg_{inter} plot referred to the cation–anion interactions.

component of the δg_{inter} descriptor for both the $PIP_{1,2O2}$DFOB and $PIP_{1,2O2}$BOB cases. A slightly more intense peak with a maximum at more negative values is obtained for the $PIP_{1,2O2}$-BOB interaction suggesting a stronger cation–anion attraction in the $PIP_{1,2O2}$BOB IL, which is in line with the weaker BOB–BOB anion–anion interaction (Fig. 5c and d) with respect to the DFOB–DFOB one (Fig. 5a and b). Altogether these findings are in good agreement among each other and in the line with our initial hypothesis about the lower T_g and T_m values of the DFOB-based ILs as compared to BOB-based ones are caused by the weaker cation–anion interactions in the former case, which in turn are due to the stronger anion–anion interaction induced by the fluorination of the anions.

4 Conclusions

Four ILs based on oxalatoborate anions were synthesized and their physico-chemical properties were investigated by experimental methods. Due to the lack of literature about structural studies on this kind of ILs, computational methods, involving the use of both MD simulations and DFT calculations, were used to gain insights on how the liquid bulk structure dictates the observed experimental features. MD simulations show that the insertion of the oxygen atom in the side chain of the cation provokes a more disordered structural distribution of the IL ions due to an increased conformational flexibility. At the same time, it is highlighted that in BOB-based ILs a more packed cation–anion distribution is present as compared to DFOB-based ILs. Weak but detectable interactions between different domains of the anions seem to occur alongside and in competition with the cation–anion ones and are stronger in the DFOB case due to a more positive charge on the boron atom of the anion, induced by the presence of fluorine atoms. This is also the origin of the lower T_g and T_m values in DFOB-based ILs. DFT calculations on cation–anion clusters were performed to assess this hypothesis, confirming that anion–anion attractive interactions are possible for both the DFOB–DFOB and BOB–BOB anions due to their highly delocalized charge. In DFOB-based ILs the anion–anion attraction is stronger, and the cation–anion one consequently weaker, in comparison to BOB-based ILs. This study shows that in the presence of large anions, such as DFOB and BOB, the anion–anion interplay cannot be neglected, and this concurs in determining the physico-chemical properties of ILs.

Author contributions

M. A. N. and P. D. conceptualized this work. M. P. and A. T. carried out the synthesis of the ionic liquids. M. P. carried out the thermal analyses, the ATR-FTIR experiments and evaluated the experimental density of the ionic liquids. G. M. carried out the MD simulations and DFT calculations. A. T. and M. B. supervised the experimental and computation aspects of this work. M. P. and G. M. wrote the original draft of this manuscript. A. T., M. B., M. A. N and P. D. revised and improved the original draft to its present form. All authors have made final approval of the original version of the manuscript.

Data availability

The data supporting this article have been included as part of the ESI.†

Conflicts of interest

The authors declare that they have no known competing financial interests or personal relationships that could have appeared to influence the work reported in this paper.

Acknowledgements

M. A. N. thanks the financial support of ENEA (Agenzia nazionale per le nuove tecnologie, l'energia e lo sviluppo economico sostenibile) to the ''Innovative electrolytes based on green ionic liquids'' project, within the PTR 2022-2024 (Piano Triennale di

Realizzazione) of the AdP (Accordo di Programma) between MASE and ENEA, CNR and RSE S.p.A. The authors acknowledge the European Union-NextGeneration EU under the Italian Ministry of University and Research 582 (MUR), Network 4 Energy Sustainable Transition NEST project (MIUR project code PE000021, CUP B53C22004070006). M. P. thanks Sapienza University of Rome for funding Progetto per Avvio alla Ricerca-Tipo 1 AR1221816B56A67B.

References

1 R. D. Rogers and K. R. Seddon, *Science*, 2003, **302**, 792–793.
2 T. Welton, *Biophys. Rev.*, 2018, **10**, 691–706.
3 M. Armand, F. Endres, D. R. MacFarlane, H. Ohno and B. Scrosati, *Nat. Mater.*, 2009, **8**, 621–629.
4 D. Freudenmann, S. Wolf, M. Wolff and C. Feldmann, *Angew. Chem., Int. Ed.*, 2011, **50**, 11050–11060.
5 Z. S. Qureshi, K. M. Deshmukh and B. M. Bhanage, *Clean Technol. Environ Policy*, 2014, **16**, 1487–1513.
6 P. Halder, S. Kundu, S. Patel, A. Setiawan, R. Atkin, R. Parthasarthy, J. Paz-Ferreiro, A. Surapaneni and K. Shah, *Renewable Sustainable Energy Rev.*, 2019, **105**, 268–292.
7 M. Zhang, V. Kamavaram and R. G. Reddy, *Min. Metall. Explor.*, 2006, **23**, 177–186.
8 J. Huang and T. Rüther, *Aust. J. Chem.*, 2009, **62**, 298.
9 F. Wu, S. Fang, M. Kuenzel, A. Mullaliu, J.-K. Kim, X. Gao, T. Diemant, G.-T. Kim and S. Passerini, *Joule*, 2021, **5**, 2177–2194.
10 F. Wu, G. Kim, T. Diemant, M. Kuenzel, A. R. Schür, X. Gao, B. Qin, D. Alwast, Z. Jusys, R. J. Behm, D. Geiger, U. Kaiser and S. Passerini, *Adv. Energy Mater.*, 2020, **10**, 2001830.
11 S. Brutti, E. Simonetti, M. De Francesco, A. Sarra, A. Paolone, O. Palumbo, S. Fantini, R. Lin, A. Falgayrat, H. Choi, M. Kuenzel, S. Passerini and G. B. Appetecchi, *J. Power Sources*, 2020, **479**, 228791.
12 J. S. Moreno, Y. Deguchi, S. Panero, B. Scrosati, H. Ohno, E. Simonetti and G. B. Appetecchi, *Electrochim. Acta*, 2016, **191**, 624–630.
13 A. Tsurumaki, H. Ohno, S. Panero and M. A. Navarra, *Electrochim. Acta*, 2019, **293**, 160–165.
14 O. Palumbo, A. Sarra, J.-B. Brubach, F. Trequattrini, A. Cimini, S. Brutti, G. B. Appetecchi, E. Simonetti, G. Maresca, S. Fantini, R. Lin, A. Falgayrat, P. Roy and A. Paolone, *Front. Phys.*, 2022, **10**, 851279.
15 F. Philippi and T. Welton, *Phys. Chem. Chem. Phys.*, 2021, **23**, 6993–7021.
16 A. Tsurumaki, M. Branchi, A. Rigano, R. Poiana, S. Panero and M. A. Navarra, *Electrochim. Acta*, 2019, **315**, 17–23.
17 Y. Jin, S. Fang, M. Chai, L. Yang and S. Hirano, *Ind. Eng. Chem. Res.*, 2012, **51**, 11011–11020.
18 K. Yoshii, T. Uto, N. Tachikawa and Y. Katayama, *Phys. Chem. Chem. Phys.*, 2020, **22**, 19480–19491.
19 K. Yoshii, T. Uto, T. Onishi, D. Kosuga, N. Tachikawa and Y. Katayama, *ChemPhysChem*, 2021, **22**, 1584–1594.
20 L. Lombardo, S. Brutti, M. A. Navarra, S. Panero and P. Reale, *J. Power Sources*, 2013, **227**, 8–14.
21 A. Celeste, L. Silvestri, M. Agostini, M. Sadd, S. Palumbo, J. K. Panda, A. Matic, V. Pellegrini and S. Brutti, *Batteries Supercaps*, 2020, **3**, 1059–1068.
22 G. Di Donato, G. Maresca, M. Palluzzi, A. Tsurumaki and M. A. Navarra, *Materials*, 2023, **16**, 1411.
23 J. Jang, J. Shin, S. Ko, H. Park, W. Song, C. B. Park and J. Kang, *Adv. Energy Mater.*, 2022, **12**, 2103955.
24 A. Tsurumaki, M. Agostini, R. Poiana, L. Lombardo, E. Lufrano, C. Simari, A. Matic, I. Nicotera, S. Panero and M. A. Navarra, *Electrochim. Acta*, 2019, **316**, 1–7.
25 M. R. Shimpi, P. Rohlmann, F. U. Shah, S. Glavatskih and O. N. Antzutkin, *Phys. Chem. Chem. Phys.*, 2021, **23**, 6190–6203.
26 J. Guzmán-Torres, D. L. Ochoa-Gamboa, L. L. Garza-Tovar, L. C. Torres-González, S. M. De La Parra-Arciniega, E. González-Juárez, I. Gómez and E. M. Sánchez, *J. Electron. Mater.*, 2023, **52**, 1250–1257.
27 T. Dubaj, A. Tsurumaki, M. Palluzzi, M. A. Navarra, A. Ciccioli, G. Dilena and S. Vecchio Ciprioti, *J. Mol. Liq.*, 2023, **390**, 123018.
28 L. Martínez, R. Andrade, E. Birgin and J. Martínez, *J. Comput. Chem.*, 2009, **30**, 2157–2164.
29 T. Darden, D. York and L. Pedersen, *J. Chem. Phys.*, 1993, **98**, 10089–10092.
30 U. Essmann, L. Perera, M. L. Berkowitz, T. Darden, H. Lee and L. G. Pedersen, *J. Chem. Phys.*, 1995, **103**, 8577–8593.
31 J. N. Canongia Lopes and A. A. H. Pádua, *J. Phys. Chem. B*, 2004, **108**, 16893–16898.
32 W. L. Jorgensen, D. S. Maxwell and J. Tirado-Rives, *J. Am. Chem. Soc.*, 1996, **118**, 11225–11236.
33 M. J. Frisch, G. W. Trucks, H. B. Schlegel, G. E. Scuseria, M. A. Robb, J. R. Cheeseman, G. Scalmani, V. Barone, G. A. Petersson, H. Nakatsuji, X. Li, M. Caricato, A. V. Marenich, J. Bloino, B. G. Janesko, R. Gomperts, B. Mennucci, H. P. Hratchian, J. V. Ortiz, A. F. Izmaylov, J. L. Sonnenberg, D. Williams-Young, F. Ding, F. Lipparini, F. Egidi, J. Goings, B. Peng, A. Petrone, T. Henderson, D. Ranasinghe, V. G. Zakrzewski, J. Gao, N. Rega, G. Zheng, W. Liang, M. Hada, M. Ehara, K. Toyota, R. Fukuda, J. Hasegawa, M. Ishida, T. Nakajima, Y. Honda, O. Kitao, H. Nakai, T. Vreven, K. Throssell, J. A. Montgomery Jr., J. E. Peralta, F. Ogliaro, M. J. Bearpark, J. J. Heyd, E. N. Brothers, K. N. Kudin, V. N. Staroverov, T. A. Keith, R. Kobayashi, J. Normand, K. Raghavachari, A. P. Rendell, J. C. Burant, S. S. Iyengar, J. Tomasi, M. Cossi, J. M. Millam, M. Klene, C. Adamo, R. Cammi, J. W. Ochterski, R. L. Martin, K. Morokuma, O. Farkas, J. B. Foresman and D. J. Fox, *Gaussian 16 Revision C.01*, Gaussian, Inc., 2016.
34 C. M. Breneman and K. B. Wiberg, *J. Comput. Chem.*, 1990, **11**, 361–373.
35 M. Busato, P. D'Angelo, A. Lapi, M. Tolazzi and A. Melchior, *J. Mol. Liq.*, 2020, **299**, 112120.
36 F. Sessa, V. Migliorati, A. Serva, A. Lapi, G. Aquilanti, G. Mancini and P. D'Angelo, *Phys. Chem. Chem. Phys.*, 2018, **20**, 2662–2675.
37 M. Busato, P. D'Angelo and A. Melchior, *Phys. Chem. Chem. Phys.*, 2019, **21**, 6958–6969.

38 M. Busato, A. Lapi, P. D'Angelo and A. Melchior, *J. Phys. Chem. B*, 2021, **125**, 6639–6648.
39 V. Migliorati, M. Busato and P. D'Angelo, *J. Mol. Liq.*, 2022, **363**, 119801.
40 V. Migliorati and P. D'Angelo, *Results Chem.*, 2023, **6**, 101202.
41 B. Hess, H. Bekker, H. J. C. Berendsen and J. G. E. M. Fraaije, *J. Comput. Chem.*, 1997, **18**, 1463–1472.
42 M. J. Abraham, T. Murtola, R. Schulz, S. Páll, J. C. Smith, B. Hess and E. Lindahl, *SoftwareX*, 2015, **1**, 19–25.
43 M. Brehm and B. Kirchner, *J. Chem. Inf. Model.*, 2011, **51**, 2007–2023.
44 W. Humphrey, A. Dalke and K. Schulten, *J. Mol. Graphics*, 1996, **14**, 33–38.
45 F. Philippi, A. Quinten, D. Rauber, M. Springborg and R. Hempelmann, *J. Phys. Chem. A*, 2019, **123**, 4188–4200.
46 K. Fumino, S. Reimann and R. Ludwig, *Phys. Chem. Chem. Phys.*, 2014, **16**, 21903–21929.
47 S. A. Katsyuba, P. J. Dyson, E. E. Vandyukova, A. V. Chernova and A. Vidiš, *Helv. Chim. Acta*, 2004, **87**, 2556–2565.
48 C. Lefebvre, J. Klein, H. Khartabil, J.-C. Boisson and E. Hénon, *J. Comput. Chem.*, 2023, **44**, 1750–1766.
49 C. Lefebvre, H. Khartabil, J. Boisson, J. Contreras-García, J. Piquemal and E. Hénon, *ChemPhysChem*, 2018, **19**, 724–735.
50 C. Lefebvre, G. Rubez, H. Khartabil, J.-C. Boisson, J. Contreras-García and E. Hénon, *Phys. Chem. Chem. Phys.*, 2017, **19**, 17928–17936.
51 Z. Fei, D. Kuang, D. Zhao, C. Klein, W. H. Ang, S. M. Zakeeruddin, M. Grätzel and P. J. Dyson, *Inorg. Chem.*, 2006, **45**, 10407–10409.
52 A. Eftekhari, Y. Liu and P. Chen, *J. Power Sources*, 2016, **334**, 221–239.
53 J. M. Pringle, J. Golding, K. Baranyai, C. M. Forsyth, G. B. Deacon, J. L. Scott and D. R. MacFarlane, *New J. Chem.*, 2003, **27**, 1504–1510.
54 M. Amereller, T. Schedlbauer, D. Moosbauer, C. Schreiner, C. Stock, F. Wudy, S. Zugmann, H. Hammer, A. Maurer, R. M. Gschwind, H.-D. Wiemhöfer, M. Winter and H. J. Gores, *Prog. Solid State Chem.*, 2014, S0079678 614000107.
55 J. L. Allen, D. W. McOwen, S. A. Delp, E. T. Fox, J. S. Dickmann, S.-D. Han, Z.-B. Zhou, T. R. Jow and W. A. Henderson, *J. Power Sources*, 2013, **237**, 104–111.
56 S. I. Lall-Ramnarine, A. Castano, G. Subramaniam, M. F. Thomas and J. F. Wishart, *Radiat. Phys. Chem.*, 2009, **78**, 1120–1125.
57 M. Kunze, S. Jeong, G. B. Appetecchi, M. Schönhoff, M. Winter and S. Passerini, *Electrochim. Acta*, 2012, **82**, 69–74.

